




## Interplay of filling fraction and coherence in symmetry broken graphene p-n junction

Arup Kumar Paul <sup>1,3</sup>, Manas Ranjan Sahu<sup>1,3</sup>, Chandan Kumar<sup>1</sup>, Kenji Watanabe <sup>2</sup>, Takashi Taniguchi <sup>2</sup> & Anindya Das<sup>1✉</sup>

Graphene p-n junction (PNJ) with co-propagating spin-valley polarized quantum Hall (QH) edges is a promising platform for studying electron interferometry. Though several conductance measurements have been attempted for such PNJs, the edge dynamics of the spin-valley symmetry broken edge states remain unexplored. In this work, we present the measurements of conductance together with shot noise, an ideal tool to unravel the dynamics, at low temperature, in a dual graphite gated hexagonal boron nitride encapsulated high mobility graphene device. The conductance data show that the symmetry broken QH edges at the PNJ follow spin selective equilibration. The shot noise results as a function of both p and n side filling factors reveal the unique dependence of the scattering mechanism. Remarkably, the scattering is found to be fully tunable from incoherent to coherent regime with the increasing number of QH edges at the PNJ, shedding crucial insights of edge dynamics.

<sup>1</sup>Department of Physics, Indian Institute of Science, Bangalore 560012, India. <sup>2</sup>National Institute for Materials Science, Namiki 1-1, Ibaraki 305-0044, Japan. <sup>3</sup>These authors contributed equally: Arup Kumar Paul, Manas Ranjan Sahu. ✉email: [anindya@iisc.ac.in](mailto:anindya@iisc.ac.in)

Ever since the realization that the charge and energy are carried by the edge states in a quantum Hall (QH) system, the interest of edge dynamics has surged both theoretically and experimentally. The understanding of edge dynamics make an electron interferometer suitable for exploring exotic phenomena like fractional statistics, quantum entanglement, and non-abelian excitations<sup>1–5</sup>. A graphene p–n junction (PNJ) naturally harboring co-propagating electron and hole-like edge states offers an ideal platform<sup>6–22</sup> to study the edge or equilibration dynamics. The equilibration of such edge states is predicted to be facilitated by inter-channel tunneling via either incoherent or coherent scattering mechanism<sup>23–31</sup> depending on the microscopic details of the interface. As suggested by Abanin and Levitov<sup>24</sup>, for a graphene PNJ interface with random disorders, the edge mixing is expected to be dominated by the incoherent process. In the opposite limit, a cleaner PNJ interface<sup>23,29,32,33</sup> is supposed to exhibit coherent scattering. A cleaner PNJ interface is also very intriguing for studying the equilibration dynamics as it has spin and valley symmetry broken polarized QH edges<sup>34–37</sup>. Although there are several conductance measurements<sup>33,38,39</sup> showing spin-selective partial equilibration of the edges, but the equilibration dynamics for symmetry broken QH edges at a PNJ is still unknown.

Shot noise is a quintessential tool to unravel the equilibration dynamics of a junction and it is usually characterized by Fano factor ( $F$ ), which is the ratio of the actual noise to its Poissonian counterpart. For coherent and incoherent scattering,  $F = (1 - t)$  and  $t(1 - t)$ , respectively<sup>24,40–43</sup>, with  $t$  being the average transmittance of the PNJ. So far, shot noise studies<sup>44,45</sup> at graphene PNJ in the QH regime have been performed on Si/SiO<sub>2</sub> substrate-based devices, where the spin–valley symmetry broken conductance plateaus are not observed and the measured Fano<sup>44,45</sup> fairly agrees with the incoherent model<sup>24</sup> due to disorder-limited interface. Besides, the shot noise measurements<sup>44,45</sup> are focused around only the filling factors  $\nu = \pm 2$  and  $\nu = \pm 6$  with no clear dependence of  $F$  on filling factors ( $\nu$ ). More importantly, there are no shot noise studies for spin–valley symmetry broken QH edges at graphene PNJ.

With this motivation, we have carried out the conductance together with shot noise measurements at a PNJ realized in a dual graphite-gated hexagonal boron nitride (hBN) encapsulated high-mobility graphene device. From the conductance measurement, we show that the spin and valley degeneracies of the edge states are completely lifted and at the PNJ the edge states undergo spin-selective partial equilibration. Our shot noise data as a function of filling factors shows the following important results: (1) The Fano strongly depends on the filling factors. It monotonically increases with  $p$  side filling factors, whereas it slowly varies with  $n$  side filling factors. (2) For lower values of  $p$  side filling factors ( $\nu_p \leq 2$ ), the variation of Fano matches well with the calculated Fano based on incoherent scattering model, whereas for higher values of  $p$  side filling factors ( $\nu_p \geq 4$ ) Fano follows the coherent scattering model. These results reveal a crossover of scattering process from incoherent to coherent regime in the equilibration of QH edges, which has not been observed in the previous shot noise studies<sup>44,45</sup>.

## Results

**Measurement setup.** The schematics of our device with the measurement setup are shown in Fig. 1a. The PNJ device is fabricated by placing an hBN-encapsulated graphene on top of two graphite gates BG1 and BG2, each of which can independently control the carrier density of one-half of the graphene (details in Supplementary Note 1 and Supplementary Fig. 1). The PNJ (width  $\sim 10 \mu\text{m}$ ) is obtained at the interface of BG1 and BG2

by applying opposite voltages to the gates. During our entire measurement, the BG1 (BG2) side is maintained as  $n$  ( $p$ ) doped, by setting gate voltage  $V_{\text{BG1}} > 0$  ( $V_{\text{BG2}} < 0$ ). When a perpendicular magnetic field is applied to the graphene, chirally opposite QH edge states co-propagating along the PNJ are created as shown by the colored arrow lines in Fig. 1a. As shown in the figure, the current ( $I_{\text{in}}$ ) injected at the  $p$ -doped region is carried by clockwise edge states towards the PNJ. After partitioning at the PNJ, the transmitted current ( $I_t$ ) at the  $n$ -doped region and reflected current ( $I_r$ ) at the  $p$ -doped region is carried by the outgoing anti-clockwise and clockwise edge states, respectively. The shot noise generated due to partitioning at the PNJ is carried by both the transmitted and reflected paths. To measure  $I_t$  and the shot noise, the measurement setup consists of two parts: (1) A low frequency ( $\sim 13$  Hz) part, which determines  $I_t$  by measuring the voltage drop  $V_m$  at the  $n$ -doped region, with a lock-in amplifier (LA) as shown in Fig. 1(a) (also see Supplementary Note 2 and Supplementary Fig. 2a). (2) A high-frequency shot noise measurement part, where a direct current (DC) current ( $I_{\text{in}}$ ) is injected at  $p$ -doped region and the generated noise is measured at reflected side using LCR resonant circuit at  $\sim 765$  kHz as shown in Fig. 1a (described in detail in Supplementary Fig. 2b). All the measurements were performed at 8 T magnetic field inside a cryo-free dilution fridge (with base temperature  $\sim 10$  mK), whose mixing chamber plate serves as the cold ground (Fig. 1a).

**Conductance measurement.** Figure 1b shows trans-resistance,  $R_t = V_m/I_{\text{in}}$  as a function of gate voltages  $V_{\text{BG1}}$  and  $V_{\text{BG2}}$ . The plot shows plateau-like features creating a checkerboard pattern for different combinations of  $p$  and  $n$  side filling factors,  $\nu_p$  and  $\nu_n$ , respectively (details in Supplementary Note 3 and Supplementary Fig. 3a). The transmittance  $t = I_t/I_{\text{in}}$  of each plateau is determined from the  $R_t$  as  $t = |\nu_n| R_t / \frac{h}{e^2}$ , where  $V_m = I_t R_h$  and  $R_h = \frac{h}{e^2} / |\nu_n|$  is the QH resistance of the  $n$ -doped region. To understand the filling factor dependence of  $t$ , we have shown the two possible sequences of spin polarization of the edge states (valley or spin-polarized ground state) in Fig. 1c<sup>39</sup>. The Fig. 1d shows the measured values of  $t$  (open circles with error bar) as function  $\nu_n$  for  $\nu_p = -1$  with the corresponding theoretical values considering full equilibration<sup>24</sup>;  $t_{\text{full}} = |\nu_n| / (|\nu_p| + |\nu_n|)$  (blue dashed line), and spin-selective partial equilibration<sup>38,39,46</sup>,  $t_{\text{spin}} = \frac{1}{|\nu_p|} \left[ \frac{|\nu_p| \nu_n|}{|\nu_p| + |\nu_n|} + \frac{|\nu_p| \nu_n|}{|\nu_p| + |\nu_n|} \right]$  (red dashed line), where  $|\nu_p| (|\nu_n|)$  and  $|\nu_n| (|\nu_n|)$  are the total number of up (down) spin edge channels of the  $p$ - and  $n$ -doped region, respectively (Supplementary Note 4 and Supplementary Fig. 4). The error bars (standard deviations) in Fig. 1d and Supplementary Fig. 4 show the conductance fluctuation of different plateaus. It can be seen that, although the conductance fluctuation increases with higher filling factor, the magnitude of the fluctuation remains negligible compared to the average transmittance values. We note that for clarity we have removed the error bars that are smaller than the width of the symbol used. The red dashed line in Fig. 1d is based on the spin structure for the spin-polarized ground state and it is in very good agreement with the measured  $t$ . Note that the other spin sequence also gives good agreement with the experimental data. For simplicity, we will be presenting only one of them (spin-polarized ground state) throughout the manuscript. The measured  $t$  and the calculated values based on spin-selective equilibration for other plateaus are also in very good agreement and are shown in Supplementary Fig. 4.

**Shot noise measurement.** In this section, we present the results of our shot noise measurement. The shot noise generated at the PNJ is measured at the reflected side ( $p$  side) as a function of  $I_{\text{in}}$ ,

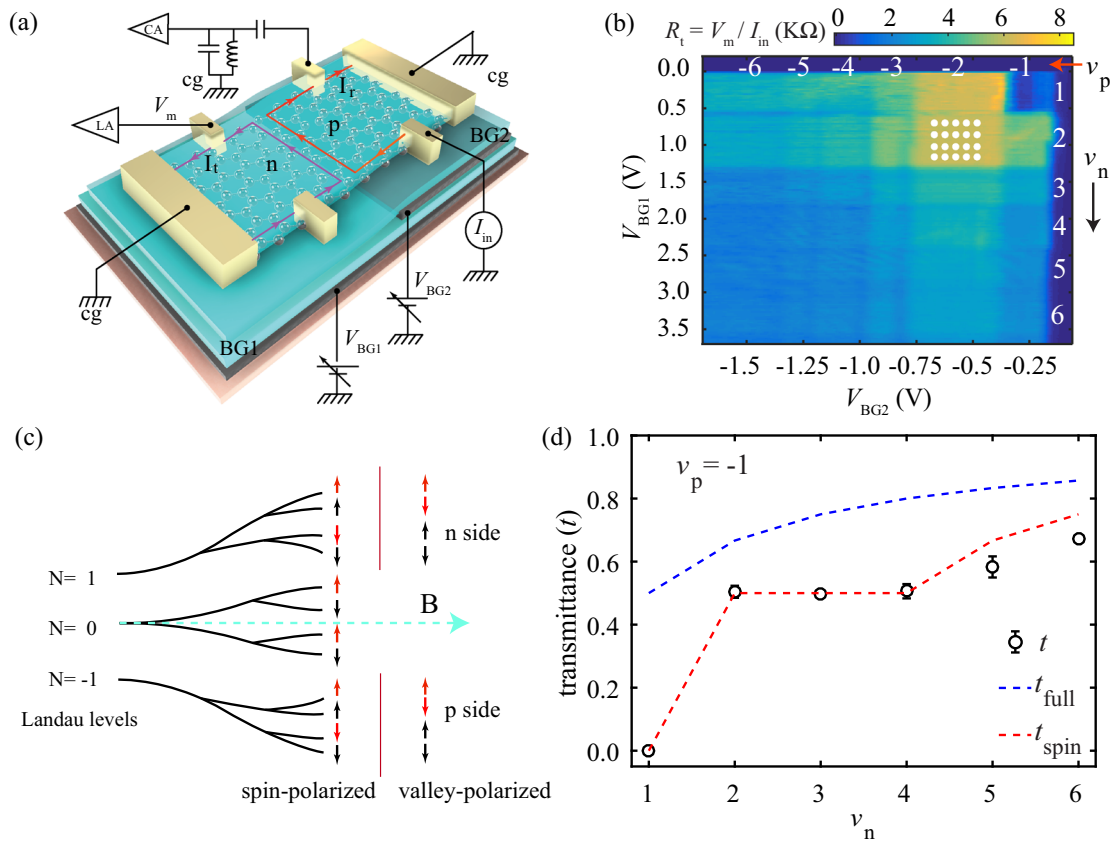


**Fig. 1 Schematics and junction transmittance.** **a** Schematics of the device and measurement setup. The encapsulated graphene flake is positioned on top of two bottom graphite gates BG1 and BG2, which are connected to the gate voltages  $V_{BG1}$  and  $V_{BG2}$ . The chirality of the edge states during measurement, for p- and n-doped region, is shown by the red and purple arrowed lines. For both conductance and shot noise measurements, excitation current  $I_{in}$  is injected at the p side. The transmitted current ( $I_t$ ) at the n side is determined by measuring the voltage  $V_m$  with a lock-in amplifier (LA). The shot noise generated at the graphene p-n junction (PNJ) is measured at the p side using a resonant tank circuit followed by a cryogenic amplifier (CA). The extreme left and right contacts were grounded to the dilution mixing chamber plate serving as cold ground (cg). **b** The trans-resistance  $R_t = V_m / I_{in}$ , as a function of  $V_{BG1}$  and  $V_{BG2}$ .  $R_t$  shows a checkerboard-like pattern corresponding to the different combinations of p and n side filling factors  $\nu_p$  and  $\nu_n$ , shown in the white vertical and horizontal axis, respectively. The white dotted points on  $(\nu_p, \nu_n) = (-2, 2)$  plateau are to show how noise data were taken at several different  $(V_{BG1}, V_{BG2})$  points of the same plateau. **c** Spin configuration of the edge states for two different ways of Landau level (LL) degeneracy lifting with increasing magnetic field ( $B$ ): spin and valley polarized ground states. Red and black color indicates valley degrees of freedom. **d** Measured transmittance  $t$  (open circles) with error bar (standard deviation of  $t$  from average value) of the PNJ as a function of filling factor  $\nu_n$  for  $\nu_p = -1$ . The calculated  $t$  for full equilibration ( $t_{full}$ ) and spin-selective equilibration ( $t_{spin}$ ) for spin-polarized ground state is shown by blue and red dashed lines, respectively.

as shown in Fig. 1a. In general, measured excess current noise ( $S_I$ ) with finite temperature broadening follows the expression:

$$S_I = 2eI_{in}F^* \left[ \coth\left(\frac{eV_{sd}}{2k_B T}\right) - \frac{2k_B T}{eV_{sd}} \right], \quad (1)$$

where  $V_{sd}$  is the applied bias voltage across the PNJ,  $T$  is the temperature, and  $k_B$  is Boltzmann constant. For  $eV_{sd} > k_B T$  shot noise dominates over thermal broadening and  $S_I$  becomes linear with  $I_{in}$ . This can be seen in Fig. 2a, showing one representative  $S_I$  versus  $I_{in}$  noise data for  $(\nu_p, \nu_n) = (-2, 2)$ ,  $(-3, 3)$ , and  $(-4, 4)$  filling factor plateaus. It should be noted that  $S_I$  is the excess current noise without the thermal equilibrium noise ( $V_{sd} = 0$ ). The red lines in Fig. 2a are the fit using Eq. (1). The slopes of the fit have been used to determine the normalized noise magnitude ( $F^* = \frac{S_I}{2eI_{in}}$ ). For obtaining Fano ( $F = \frac{S_I}{2eI_{in}}$ ), we just follow  $F = F^*/t$ , which is conventionally used to characterize the noise and used in the previous shot noise studies on graphene PNJ<sup>44,45</sup>. Figure 2b shows the histogram of  $F$  values, obtained from the noise data taken at several  $(V_{BG1}, V_{BG2})$  points ( $\sim 50$ ) (Supplementary Note 5) on each checkerboard (plateau) as shown by the white dotted points in Fig. 1b for  $(\nu_p, \nu_n) = (-2, 2)$ . The histograms are

fitted with the Gaussian function as shown by the solid red lines in Fig. 2b for  $(\nu_p, \nu_n) = (-2, 2)$ ,  $(-3, 3)$ , and  $(-4, 4)$  plateaus. It can be seen that the histograms have a maximum at a certain value of  $F$  (mean value), which depends on the filling factors  $(\nu_p, \nu_n)$ . The noise data and the corresponding histograms for some other plateaus are shown in Supplementary Figs. 5, 6, and 7. The variation in Fano is well captured by the Gaussian function for most of the plateaus, except for some plateaus with large Fano variation. To quantify how well the Gaussian fitting is, we have quoted the “R-squared” value of the fitting (also see Supplementary Figs. 6 and 7). We should note that the accuracy of the extracted Fano is very essential to pinpoint the exact scattering mechanism. The accuracy also depends on the amplifier gain and noise from the contacts, as well as on enough statistics. In Supplementary Note 6 and Supplementary Fig. 8, the precise gain calibration and in Supplementary Note 7 and Supplementary Fig. 9, the measured contact noise as a function filling factors are described. The contact noise has been subtracted in the histogram plots shown in Fig. 2b as well as in Supplementary Figs. 6 and 7.

The measured values of  $F$  (mean value) as a function of filling factor are shown in Fig. 3 as open circles with the error bars (standard deviations of Gaussian fit in Fig. 2b). In Fig. 3a, b,  $F$  is

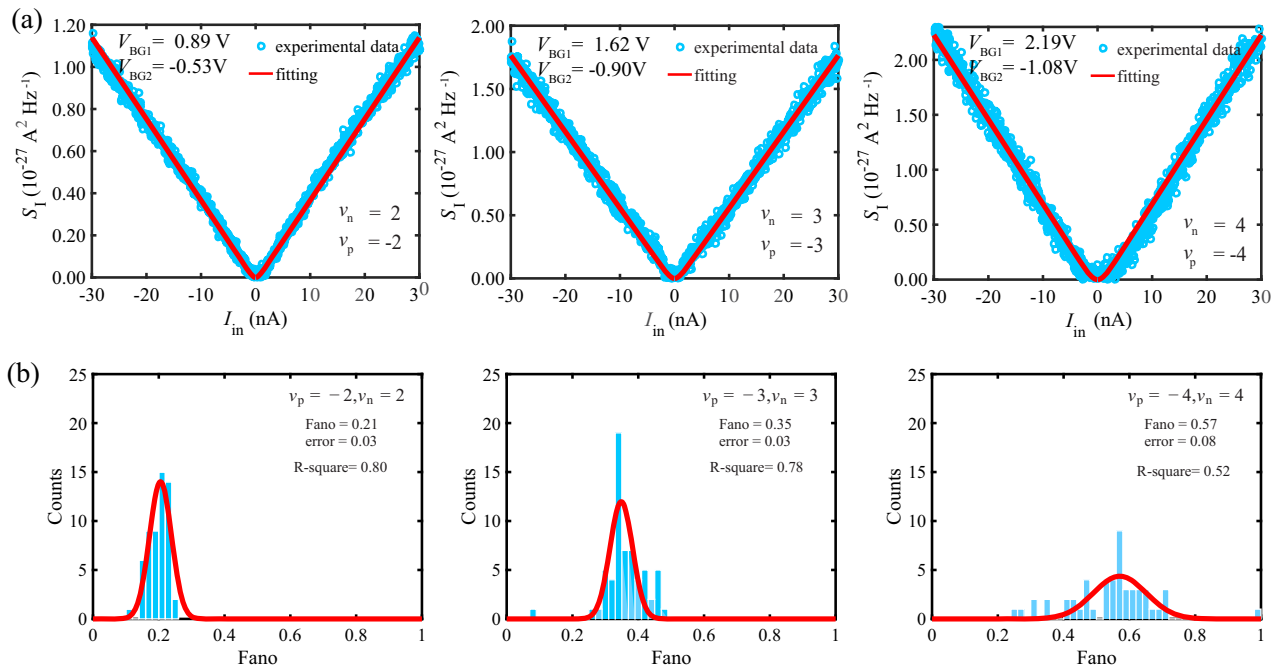


**Fig. 2 Shot noise and Fano factor.** **a** Measured current noise ( $S_I$ ) generated by the graphene p-n junction (PNJ), as a function of injected current  $I_{in}$ , for filling factor  $(\nu_p, \nu_n) = (2, -2), (3, -3)$  and  $(4, -4)$  plateaus. The gate voltage values ( $V_{BG1}, V_{BG2}$ ), at which the data have been taken are shown in the figures. The solid red lines are the fit with Eq. (1) to extract the Fano factor. **b** Histogram of all Fano values obtained from noise data taken at several ( $V_{BG1}, V_{BG2}$ ) points ( $\sim 50$ ) for the  $(\nu_p, \nu_n) = (2, -2), (3, -3)$  and  $(4, -4)$  plateaus. The solid lines are the Gaussian fit to extract the mean value of  $F$  and error is its standard deviation. The  $R$ -squared value shows the quality of the fitting.

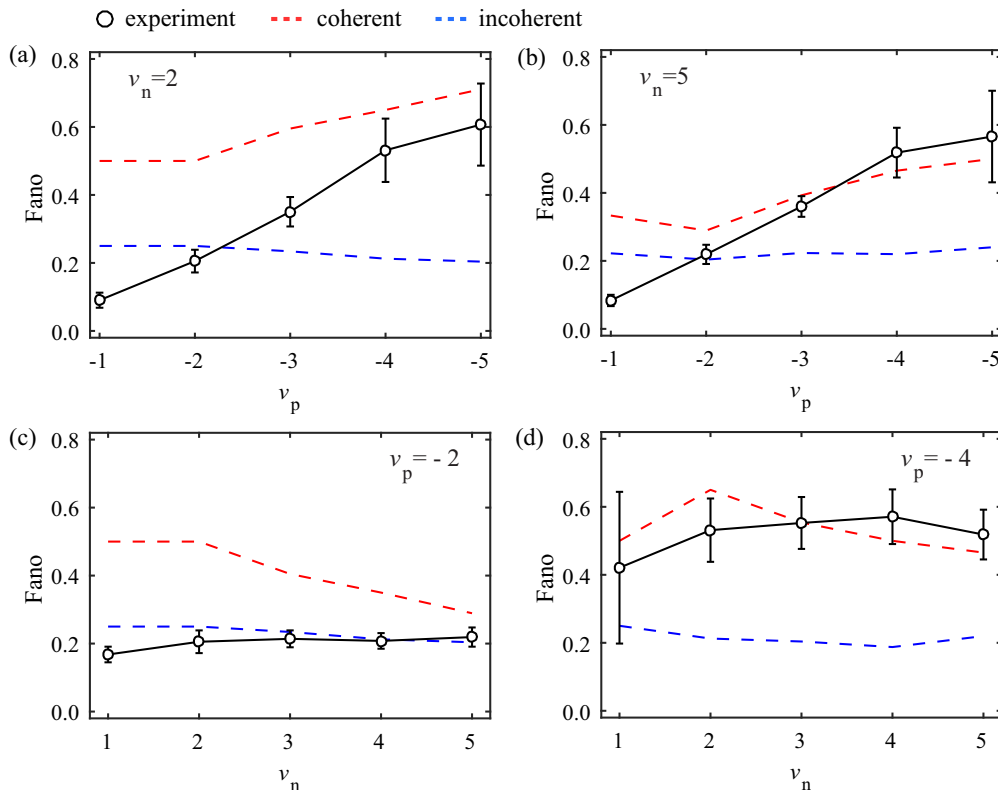


**Fig. 3 Fano versus filling factor.** Fano as a function of p side filling factor  $\nu_p$ , for n side filling factor  $\nu_n = 2$  (**a**) and  $\nu_n = 5$  (**b**). Open circles with error bars represent the experimentally measured Fano. The error bars correspond to the standard deviation from the Gaussian fits of the Fano histograms. Red and blue dashed lines correspond to the theoretically calculated Fano for coherent and incoherent scattering (quasi-elastic), respectively. **c, d** shows Fano as a function of filling factor  $\nu_n$  for  $\nu_p = -2$  and  $\nu_p = -4$ , respectively. Red and blue dashed lines correspond to the calculated Fano for coherent and incoherent scattering (quasi-elastic), respectively.

plotted as a function of  $\nu_p$ , while the n side filling factor is kept fixed at  $\nu_n = 2$  and  $\nu_n = 5$ , respectively. It can be seen that  $F$  increases monotonically from  $\sim 0.05$  to  $0.6$  with increasing  $\nu_p$ . Similarly, in Fig. 3c, d,  $F$  is plotted as a function of  $\nu_n$ , while the p side filling factor is kept fixed at  $\nu_p = -2$  and  $\nu_p = -4$ , respectively. However, in this case, the  $F$  does not increase monotonically with  $\nu_n$ , rather slowly varies around  $\sim 0.2$  and  $0.6$  for  $\nu_p = -2$  and  $\nu_p = -4$ , respectively. A similar dependence of  $F$  on  $\nu_n$  or  $\nu_p$  for other fixed values of  $\nu_p$  or  $\nu_n$  (Supplementary Note 8) are shown in Supplementary Figs. 10 and 11.

## Discussion

To understand the above results, we theoretically calculate  $F$  for coherent and incoherent processes. In coherent scattering, the injected hot carriers from p side (Fig. 1a) coherently scatter to the n side and the inter-channel scattering can be described by scattering matrix approach<sup>40,41</sup>. In this case,  $F$  follows as  $(1 - t)$  similar to that of a quantum point contact (details in Supplementary Note 9). Furthermore, for our symmetry broken PNJ, we also impose the constraints that the two opposite spin channels do not interact with each other<sup>39,46</sup>. Thus, the Fano can be written as  $F_{\text{coherent}} = (|\nu_{p\uparrow}|t_{\uparrow}(1 - t_{\uparrow}) + |\nu_{p\downarrow}|t_{\downarrow}(1 - t_{\downarrow})) / (|\nu_{p\uparrow}|t_{\uparrow} + |\nu_{p\downarrow}|t_{\downarrow})$ , where  $t_{\uparrow} = |\nu_{n\uparrow}| / (|\nu_{n\uparrow}| + |\nu_{p\uparrow}|)$  and  $t_{\downarrow} = |\nu_{n\downarrow}| / (|\nu_{n\downarrow}| + |\nu_{p\downarrow}|)$  are the transmittance of up and down spin channels, respectively (Supplementary Note 4). The calculated  $F_{\text{coherent}}$  is shown as red dashed lines in Fig. 3.  $F_{\text{coherent}}$  increases with  $\nu_p$  but decreases with  $\nu_n$ , which can be qualitatively understood as the transmittance of the PNJ decreases and increases with  $\nu_p$  and  $\nu_n$ , respectively. For incoherent scattering, we consider the quasi-elastic<sup>24,41</sup> scattering. In quasi-elastic case, known as chaotic cavity model, the injected hot carriers from p side scatters to the n side and subsequently scatters back and forth due to the presence of disorders along the PNJ giving rise to double-step distribution<sup>24,41,43,44,47,48</sup>. Following Abanin and Levitov<sup>24</sup> the expression for  $F$  is  $t(1 - t)$  and for our symmetry broken PNJ Fano can be written as  $F_{\text{incoherent}} = (|\nu_{p\uparrow}|t_{\uparrow}^2(1 - t_{\uparrow}) + |\nu_{p\downarrow}|t_{\downarrow}^2(1 - t_{\downarrow})) / (|\nu_{p\uparrow}|t_{\uparrow} + |\nu_{p\downarrow}|t_{\downarrow})$ . The calculated  $F_{\text{incoherent}}$  is shown as blue dashed lines in Fig. 3 (Supplementary Note 9).  $F_{\text{incoherent}}$  remain almost constant around  $F \sim 0.2$  and much smaller in magnitude compared to  $F_{\text{coherent}}$ . For the completeness, we also mention the Fano values for inelastic scattering as described by Abanin and Levitov<sup>24</sup>, which is very similar in magnitude with the quasi-elastic case as shown in Supplementary Fig. 16e.

The monotonic increase of  $F$  with  $\nu_p$  in Fig. 3a, b is in contradiction with the incoherent scattering model and is consistent with the coherent case, except for lower values of  $\nu_p$ . However, the measured  $F$  with  $\nu_n$  for  $\nu_p = -2$  matches very well with the incoherent scattering, but for  $\nu_p = -4$  it perfectly matches the coherent model. This suggests there is a crossover from incoherent to the coherent regime with the increasing number of edge channels at the p side. This is also seen in Fig. 4, where the measured  $F$  plotted as a function of  $|\nu_p| = |\nu_n|$  and increases monotonically from  $\sim 0.2$  to  $0.55$  (open circles), whereas  $F_{\text{incoherent}}$  (blue dashed line) and  $F_{\text{coherent}}$  (red dashed line) remain constant around  $\sim 0.25$  and  $0.5$ , respectively. The coherent nature is further manifested as an increase in Fano error bar, showing a wider spread of Fano values at higher filling factors. This can be qualitatively understood from the increased mesoscopic conductance fluctuations of the junction, observed at higher filling factors plateaus. As the coherence increases, conductance fluctuation increases<sup>23,31</sup>, as can be seen in Fig. 1b, d.

One plausible reason for the observed crossover with increasing filling factor is the velocity-dependent phase coherence of the edge states<sup>49</sup>. The velocity, hence the phase coherence of the edge states, increases with a higher filling factor, as the confining

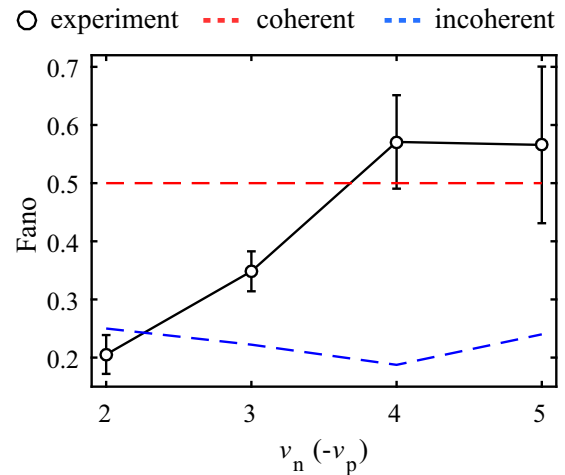


**Fig. 4 Crossover from incoherent to coherent regime.** Fano (open circle with error bars) as a function of n or p side filling factors  $\nu_n$  or  $\nu_p$ , when  $|\nu_n| = |\nu_p|$ . The error bars correspond to the standard deviation of the Gaussian fits to the Fano histograms. Red and blue dashed lines correspond to the theoretically calculated Fano for coherent and incoherent scattering (quasi-elastic), respectively. The crossover from incoherent to coherent regime can be seen with increasing filling factors.

potential becomes steeper. It qualitatively explains the observed crossover from incoherent to coherent scattering regime with increasing filling factor. Also, the asymmetric dependence of the Fano factor on p and n side filling factors (Fig. 3) can be qualitatively understood, by considering different steepness of the confining potential on either side of the PNJ<sup>14</sup>. In our device, the graphite gate BG2 is closer ( $\sim 21$  nm) to the graphene flake, than the graphite gate BG1 ( $\sim 50$  nm). Hence, at the p-doped side of the junction the confinement potential is steeper compared to that at n-doped side. As a result, the phase coherence of the edge states at the p side will change more rapidly than that for edge states at the n side. One more possibility could be that the screening might be playing a big role in dynamics as observed in GaAs-based two-dimensional electron gas<sup>47,50–53</sup>. The coherent scattering dominates as the screening increases with more number of participating edges at the PNJ. However, it does not explain the asymmetry observed in Fig. 3.

In summary, we have carried out conductance together with shot noise measurement on a high-quality graphene PNJ, for the first time, with spin and valley symmetry broken QH edges. We have shown that the conductance data follows the spin-selective partial equilibration, and most importantly, our shot noise data reveal the intricate dependence of Fano on filling factors with a crossover in dynamics from incoherent to the coherent regime, which cannot be obtained from the conductance measurements. These results will help to design future electron optics experiments using the polarized QH edges of graphene.

## Methods

**Device fabrication.** To make the encapsulated device, the hBN and graphene, as well as the graphite flakes for bottom gates, were exfoliated from bulk crystals on Si/SiO<sub>2</sub> substrates. Natural graphite crystals were used for exfoliating graphene and the graphite flakes. The suitable flakes for the device were first identified under an optical microscope and then sequentially assembled with the residue-free poly-carbonate-polydimethylsiloxane stamp technique<sup>54–56</sup>. We have used 15- and 21-nm-thick hBN flakes for encapsulating the graphene flake and 10–15-nm-thick graphite flakes for the bottom gates. To make the metal edge contacts on the device, first, the contacts were defined with e-beam lithography technique. Then, along the defined region, only the top hBN flake was etched out using CHF<sub>3</sub>–O<sub>2</sub> plasma. After that Cr(2 nm)/Pd(10 nm)/Au(70 nm) was deposited using thermal evaporation.



**Shot noise setup.** To measure the shot noise, first, the voltage noise generated from the device is filtered by a superconducting resonant LC tank circuit, with resonance frequency at 765 kHz and bandwidth 30 kHz<sup>57,58</sup>. The filtered signal is then further amplified by the HEMT cryo amplifier followed by a room temperature amplifier. The amplified signal is then fed to a spectrum analyzer, to measure the root mean square of the signal. The gain of the amplifier chain is determined from the temperature dependence of the thermal noise of  $\nu_p = -2$  filling factor plateau, while the n side is in the insulating state. The thermal noise measurement is carried out using the same noise circuit.

### Data availability

The authors declare that the main data supporting the findings of this study are available within the article and its Supplementary information file. Any other related data are available from the corresponding author upon request.

Received: 13 May 2020; Accepted: 25 August 2020;

Published online: 01 October 2020

### References

- Neder, I., Heiblum, M., Levinson, Y., Mahalu, D. & Umansky, V. Unexpected behavior in a two-path electron interferometer. *Phys. Rev. Lett.* **96**, 016804 (2006).
- Neder, I. et al. Interference between two indistinguishable electrons from independent sources. *Nature* **448**, 333–337 (2007).
- Law, K. T., Feldman, D. & Gefen, Y. Electronic mach-zehnder interferometer as a tool to probe fractional statistics. *Phys. Rev. B* **74**, 045319 (2006).
- Feldman, D. & Kitaev, A. Detecting non-abelian statistics with an electronic mach-zehnder interferometer. *Phys. Rev. Lett.* **97**, 186803 (2006).
- Stern, A. Non-abelian states of matter. *Nature* **464**, 187–193 (2010).
- Zhang, Y., Tan, Y.-W., Stormer, H. L. & Kim, P. Experimental observation of the quantum hall effect and berry's phase in graphene. *Nature* **438**, 201–204 (2005).
- Neto, A. C., Guinea, F., Peres, N. M., Novoselov, K. S. & Geim, A. K. The electronic properties of graphene. *Rev. Mod. Phys.* **81**, 109 (2009).
- Abanin, D. A., Lee, P. A. & Levitov, L. S. Spin-filtered edge states and quantum hall effect in graphene. *Phys. Rev. Lett.* **96**, 176803 (2006).
- Özyilmaz, B. et al. Electronic transport and quantum hall effect in bipolar graphene p-n-p junctions. *Phys. Rev. Lett.* **99**, 166804 (2007).
- Williams, J., DiCarlo, L. & Marcus, C. Quantum hall effect in a gate-controlled pn junction of graphene. *Science* **317**, 638–641 (2007).
- Milovanović, S., Ramezani Masir, M. & Peeters, F. Interplay between snake and quantum edge states in a graphene hall bar with a pn-junction. *Appl. Phys. Lett.* **105**, 123507 (2014).
- Rickhaus, P. et al. Snake trajectories in ultraclean graphene p–n junctions. *Nat. Commun.* **6**, 1–6 (2015).
- Taychatanapat, T. et al. Conductance oscillations induced by ballistic snake states in a graphene heterojunction. *Nat. Commun.* **6**, 1–6 (2015).
- Klimov, N. N. et al. Edge-state transport in graphene p-n junctions in the quantum hall regime. *Phys. Rev. B* **92**, 241301 (2015).
- Kolasiński, K., Mreńca-Kolasińska, A. & Szafran, B. Imaging snake orbits at graphene n-p junctions. *Phys. Rev. B* **95**, 045304 (2017).
- Le, S. T. et al. Strong equilibration of landau levels edge-states at the graphene edge. Preprint at <https://arxiv.org/abs/1904.04726> (2019).
- Handschin, C. et al. Giant valley-isospin conductance oscillations in ballistic graphene. *Nano Lett.* **17**, 5389–5393 (2017).
- Nakaharai, S., Williams, J. & Marcus, C. Gate-defined graphene quantum point contact in the quantum hall regime. *Phys. Rev. Lett.* **107**, 036602 (2011).
- Dubey, S. & Deshmukh, M. M. Tuning equilibration of quantum hall edge states in graphene—role of crossed electric and magnetic fields. *Solid State Commun.* **237**, 59–63 (2016).
- Tóvári, E. et al. Gate-controlled conductance enhancement from quantum hall channels along graphene p–n junctions. *Nanoscale* **8**, 19910–19916 (2016).
- Makk, P. et al. Coexistence of classical snake states and aharonov-bohm oscillations along graphene p-n junctions. *Phys. Rev. B* **98**, 035413 (2018).
- Veyrat, L. et al. Low-magnetic-field regime of a gate-defined constriction in high-mobility graphene. *Nano Lett.* **19**, 635–642 (2019).
- Tworzydło, J., Snyman, I., Akhmerov, A. & Beenakker, C. Valley-isospin dependence of the quantum hall effect in a graphene p-n junction. *Phys. Rev. B* **76**, 035411 (2007).
- Abanin, D. & Levitov, L. Quantized transport in graphene pn junctions in a magnetic field. *Science* **317**, 641–643 (2007).
- Li, J. & Shen, S.-Q. Disorder effects in the quantum Hall effect of graphene p-n junctions. *Phys. Rev. B* **78**, 205308 (2008).
- Long, W., Sun, Q.-f. & Wang, J. Disorder-induced enhancement of transport through graphene p-n junctions. *Phys. Rev. Lett.* **101**, 166806 (2008).
- Low, T. Ballistic-ohmic quantum hall plateau transition in a graphene p-n junction. *Phys. Rev. B* **80**, 205423 (2009).
- Chen, J.-c., Zhang, H., Shen, S.-Q. & Sun, Q.-f. Dephasing effect on transport of a graphene p–n junction in a quantum hall regime. *J. Phys. Condens. Matter* **23**, 495301 (2011).
- Fräßdorf, C., Trifunovic, L., Bogdanoff, N. & Brouwer, P. W. Graphene p n junction in a quantizing magnetic field: conductance at intermediate disorder strength. *Phys. Rev. B* **94**, 195439 (2016).
- LaGasse, S. W. & Lee, J. U. Theory of landau level mixing in heavily graded graphene p-n junctions. *Phys. Rev. B* **94**, 165312 (2016).
- Ma, Q., Parmentier, F. D., Roulleau, P. & Fleury, G. Graphene n-p junctions in the quantum hall regime: numerical study of incoherent scattering effects. *Phys. Rev. B* **97**, 205445 (2018).
- Morikawa, S. et al. Edge-channel interferometer at the graphene quantum hall pn junction. *Appl. Phys. Lett.* **106**, 183101 (2015).
- Wei, D. S. et al. Mach-zehnder interferometry using spin-and valley-polarized quantum hall edge states in graphene. *Sci. Adv.* **3**, e1700600 (2017).
- Zhang, Y. et al. Landau-level splitting in graphene in high magnetic fields. *Phys. Rev. Lett.* **96**, 136806 (2006).
- Jiang, Z., Zhang, Y., Stormer, H. & Kim, P. Quantum hall states near the charge-neutral dirac point in graphene. *Phys. Rev. Lett.* **99**, 106802 (2007).
- Young, A. F. et al. Spin and valley quantum hall ferromagnetism in graphene. *Nat. Phys.* **8**, 550–556 (2012).
- Young, A. et al. Tunable symmetry breaking and helical edge transport in a graphene quantum spin hall state. *Nature* **505**, 528–532 (2014).
- Zimmermann, K. et al. Tunable transmission of quantum hall edge channels with full degeneracy lifting in split-gated graphene devices. *Nat. Commun.* **8**, 14983 (2017).
- Amet, F., Williams, J., Watanabe, K., Taniguchi, T. & Goldhaber-Gordon, D. Selective equilibration of spin-polarized quantum hall edge states in graphene. *Phys. Rev. Lett.* **112**, 196601 (2014).
- Büttiker, M. Scattering theory of current and intensity noise correlations in conductors and wave guides. *Phys. Rev. B* **46**, 12485 (1992).
- Texier, C. & Büttiker, M. Effect of incoherent scattering on shot noise correlations in the quantum hall regime. *Phys. Rev. B* **62**, 7454 (2000).
- Blanter, Y. M. & Büttiker, M. Shot noise in mesoscopic conductors. *Phys. Rep.* **336**, 1–166 (2000).
- Oberholzer, S. et al. Shot noise by quantum scattering in chaotic cavities. *Phys. Rev. Lett.* **86**, 2114–2117 (2001).
- Kumada, N., Parmentier, F., Hibino, H., Glatli, D. & Roulleau, P. Shot noise generated by graphene p–n junctions in the quantum hall effect regime. *Nat. Commun.* **6**, 8068 (2015).
- Matsuo, S. et al. Edge mixing dynamics in graphene p–n junctions in the quantum hall regime. *Nat. Commun.* **6**, 8066 (2015).
- Kumar, C., Srivastav, S. K. & Das, A. Equilibration of quantum hall edges in symmetry-broken bilayer graphene. *Phys. Rev. B* **98**, 155421 (2018).
- Le Sueur, H. et al. Energy relaxation in the integer quantum hall regime. *Phys. Rev. Lett.* **105**, 056803 (2010).
- Altimiras, C. et al. Non-equilibrium edge-channel spectroscopy in the integer quantum hall regime. *Nat. Phys.* **6**, 34–39 (2010).
- Nakamura, J. et al. Aharonov–bohm interference of fractional quantum hall edge modes. *Nat. Phys.* **15**, 563–569 (2019).
- Altimiras, C. et al. Tuning energy relaxation along quantum Hall channels. *Phys. Rev. Lett.* **105**, 226804 (2010).
- Gurman, I., Sabo, R., Heiblum, M., Umansky, V. & Mahalu, D. Dephasing of an electronic two-path interferometer. *Phys. Rev. B* **93**, 121412 (2016).
- Ofek, N. et al. Role of interactions in an electronic fabry–perot interferometer operating in the quantum hall effect regime. *Proc. Natl Acad. Sci. USA* **107**, 5276–5281 (2010).
- Zhang, Y. et al. Distinct signatures for coulomb blockade and aharonov-bohm interference in electronic fabry–perot interferometers. *Phys. Rev. B* **79**, 241304 (2009).
- Purdie, D. et al. Cleaning interfaces in layered materials heterostructures. *Nat. Commun.* **9**, 5387 (2018).
- Pizzocchero, F. et al. The hot pick-up technique for batch assembly of van der waals heterostructures. *Nat. Commun.* **7**, 1–10 (2016).
- Zomer, P., Guimarães, M., Brant, J., Tombros, N. & Van Wees, B. Fast pick up technique for high quality heterostructures of bilayer graphene and hexagonal boron nitride. *Appl. Phys. Lett.* **105**, 013101 (2014).
- Sahu, M. R. et al. Enhanced shot noise at bilayer graphene–superconductor junction. *Phys. Rev. B* **100**, 235414 (2019).
- Srivastav, S. K. et al. Universal quantized thermal conductance in graphene. *Sci. Adv.* **5**, eaaw5798 (2019).

## Acknowledgements

We thank Dr. Sumilan Banerjee and Dr. Tanmoy Das for the valuable comments. A.D. thanks DST (DSTO-2051) and acknowledges the Swarnajayanti Fellowship of the DST/SJF/PSA-03/2018-19 for the financial support. K.W. and T.T. acknowledge support from the Elemental Strategy Initiative conducted by the MEXT, Japan and the CREST (JPMJCR15F3), JST.

## Author contributions

A.K.P. and M.R.S. contributed to device fabrication, data acquisition, and analysis. C.K. contributed to the noise setup and preliminary experiments. A.D. contributed to conceiving the idea and designing the experiment, data interpretation, and analysis. K.W. and T.T. synthesized the hBN single crystals. All authors contributed to writing the manuscript.

## Competing interests

The authors declare no competing interests

## Additional information

**Supplementary information** is available for this paper at <https://doi.org/10.1038/s42005-020-00434-x>.

**Correspondence** and requests for materials should be addressed to A.D.

**Reprints and permission information** is available at <http://www.nature.com/reprints>

**Publisher's note** Springer Nature remains neutral with regard to jurisdictional claims in published maps and institutional affiliations.



**Open Access** This article is licensed under a Creative Commons Attribution 4.0 International License, which permits use, sharing, adaptation, distribution and reproduction in any medium or format, as long as you give appropriate credit to the original author(s) and the source, provide a link to the Creative Commons license, and indicate if changes were made. The images or other third party material in this article are included in the article's Creative Commons license, unless indicated otherwise in a credit line to the material. If material is not included in the article's Creative Commons license and your intended use is not permitted by statutory regulation or exceeds the permitted use, you will need to obtain permission directly from the copyright holder. To view a copy of this license, visit <http://creativecommons.org/licenses/by/4.0/>.

© The Author(s) 2020